Swept Transition Experimental Platform (STEP)

Rius Vidales, A.F.; Barahona Lopez, M.; Kotsonis, M.

DOI
10.2514/6.2024-0942

Publication date
2024

Document Version
Final published version

Published in
Proceedings of the AIAA SCITECH 2024 Forum

AIAA SciTech Forum
8-12 January 2024, Orlando, FL
AIAA SCITECH 2024 Forum

10.2514/6.2024-0942

Swept Transition Experimental Platform (STEP)

Alberto F. Rius-Vidales * †, Marina Barahona ‡ and Marios Kotsonis§
Delft University of Technology, 2629 HS Delft, The Netherlands

A new experimental facility named Swept Transition Experimental Platform (STEP) has been designed and built for detailed studies of crossflow instability and its interaction with surface irregularities and varying wall temperature conditions. The STEP is designed for use in the anechoic low-turbulence wind tunnel facility at the Delft University of Technology (TU Delft). The new facility consists of a swept flat-plate model with a movable leading edge capable of precisely translating to create forward/backward-facing step irregularities. In addition, the plate's wall temperature can be adjusted to study the potential of thermal laminar flow control. An adjustable pressure body provides the favorable pressure distribution required to enhance the development of crossflow instability. Static pressure measurements are conducted to characterize the nominal pressure distribution. In addition, detailed hot-wire measurements and theoretical stability calculations reveal that the combination of discrete roughness elements, pressure distribution, and experimental facility allows for a detailed study of the development of crossflow instability in the linear and non-linear growth regime. Consequently, the STEP enables further fundamental research on laminar flow control at TU Delft.

Nomenclature

A_M	=	Steady disturbance maximum amplitude.
a	=	Unsteady disturbance amplitude.
a^*	=	Filtered unsteady disturbance amplitude.
B_H, B_L	=	High and Low frequency bands.
b	=	Flat-plate span in the Z-direction.
C_p	=	Pressure coefficient.
c_x, c_X	=	Wing chord in x and X direction.
d_D	=	Discrete roughness elements diameter.
f_s	=	Sampling frequency.
k_D	=	Discrete roughness elements height.
N	=	Disturbance amplification factor.
P	=	Power spectral density.
P^*	=	Non-dimensional PSD
Q	=	Velocity measured by the Hot-wire.
$\bar{Q}$	=	Time-averaged velocity.
Q_z	=	Spanwise averaged velocity.
Q_e	=	Velocity at boundary-layer edge.
Q_f	=	Band-pass filtered velocity.
$\langle\rangle_z$	=	Spanwise root mean square.
$\hat{q}$	=	Perturbation.
Re_{c_X}	=	Reynolds number.
R_q	=	Root mean square surface roughness.
Tu	=	Turbulence intensity.
U_∞	=	Reference freestream velocity.
U, V, W	=	Wind tunnel oriented velocity.
u, v, w	=	Leading edge oriented velocity.
X, Y, Z	=	Wind tunnel reference system.
x, y, z	=	Leading edge reference system.
s_D	=	Discrete roughness elements location.
α	=	Wavenumber along x
β	=	Wavenumber along z
δ^*	=	displacement thickness.
δ^*_Q	=	Reference displacement thickness.
$\lambda_{z,D}$	=	Spanwise wavelength DREs.
ν	=	Kinematic viscosity of air.
σ	=	Temporal standard deviation.
θ	=	Boundary-layer momentum thickness.
CF	=	Crossflow.
CFI	=	Crossflow Instability.
DRE	=	Discrete Roughness Element.
HWA	=	Hot-Wire Anemometry.
LFC	=	Laminar Flow Control.
LPSE	=	Linear Parabolized Stability Equations.
STEP	=	Swept Transition Experimental Platform.

*Email for correspondence: a.f.riusvidales@tudelft.nl
†Postdoctoral Researcher, Department of Flow Physics and Technology, Faculty of Aerospace Engineering
‡Doctoral Candidate, Department of Flow Physics and Technology, Faculty of Aerospace Engineering.
§Full Professor, Department of Flow Physics and Technology, Faculty of Aerospace Engineering..

I. Introduction

Developing and applying Laminar Flow Control (LFC) is critical for reducing the total drag in high-subsonic transport aircraft. LFC aims to stabilize the laminar boundary layer flow to delay its transition to turbulence. Doing so increases the laminar flow regions on the aircraft's surface and reduces the skin-friction drag. A reduction in this drag component directly impacts the aircraft's performance given that it is a significant contributor to the total drag [see 1, 2].

Attractive candidates for applying LFC are the wing and the horizontal/vertical tail of the aircraft. Depending on the wing geometry and airfoil shape, the laminar-turbulent transition in the boundary layer flow is driven by either one or a combination of attachment line contamination/instabilities, Görtler vortices, Tollmien-Schlichting Waves and crossflow (CF) instability [see 3]. Fortunately, through an adequate design of the airfoil geometry and pressure distribution, the first three types of instabilities can be controlled [3]. Thus, controlling CF instability is a remaining topic of interest for applying LFC in swept aerodynamic surfaces.

The primary CF instability manifests as a series of co-rotating vortices in the boundary layer. Depending on a combination of the turbulence level in the freestream flow and surface roughness, this crossflow (CF) vortices can either travel along the span or remain fixed to the surface [see 4, 5]. The breakdown of these CF vortices occurs through high-frequency secondary CF instability modes, which originate from strong shear layers generated in the spanwise modulated boundary layer flow. Several experimental and numerical studies have been dedicated to the detailed study of the CF instability [e.g. 4–8].

Experimental studies have used two approaches to replicate CF instability in laboratory conditions. The first approach uses a highly swept wing with an adequate pressure distribution (i.e., favorable pressure gradient). This approach is well-established and has been widely used [e.g. 6, 9–13]. The second approach combines the use of a highly swept flat-plate with a contoured wall or airfoil to create the pressure distribution necessary to develop CF instability [e.g. 4, 14–18].

In fundamental studies, the advantage of the flat-plate over the swept wing models is the possibility of adjusting the desired pressure distribution and the lack of surface curvature, simplifying the boundary layer measurements and baseflow/stability calculations. With this in mind and based on the combined experience in the experimental study of CF instability, the authors embarked on designing and manufacturing a new experimental facility known as the Swept Transition Experimental Platform (STEP).

The objective of the STEP is to extend the research capabilities for the recently re-furbished low-turbulence anechoic A-tunnel at the Delft University of Technology (TU Delft) by enabling detailed studies of the interaction of surface irregularities and the effects of LFC techniques on the development of primary and secondary CF instability. In comparison to the existing M3J swept wing model, extensively used at the Low Turbulence Tunnel (LTT) by the authors' research group [e.g. 6, 19–21], the STEP offers the advantage of having no surface curvature, full optical access, modularity for LFC devices and flexibility on the imposed pressure distribution.

This work presents detailed measurements of the STEP boundary-layer flow at nominal conditions. The paper structure is as follows: Sec. II describes the wind tunnel facility, experimental platform, and flow measurement techniques. Sec. III presents the development of primary and secondary CF instability. Finally, concluding remarks are presented in Sec. IV.

II. Methodology

A. Low-turbulence anechoic wind tunnel

The wind tunnel used for this investigation is a newly re-designed anechoic facility at the TU Delft. A cross-sectional diagram of the main components of this vertically arranged facility is shown in Fig. 1(a). Details of this subsonic open-jet closed-circuit wind tunnel are presented by Merino-Martinez et al. [22].

An essential aspect of this facility is the anechoic test chamber (1 in Fig. 1a), where the Swept Transition Experimental Platform (STEP) is located. At this chamber's exit (2), airflow is driven through a collector using two 30 kW centrifugal fans located outside the test chamber. From the top floor of this building, the airflow is directed toward the settling chamber (3), where it goes through a straightener and four anti-turbulence screens before reaching the cylindrical contraction (4). Different interchangeable nozzles can be used at the contraction's exit depending on the testing requirement [see 22]. In this work, a rectangular nozzle of 25×100 cm^2 is installed and directly connected to the STEP as shown in Fig. 1(b). According to Merino-Martinez et al. [22], the contraction ratio until the exit of the rectangular nozzle is 17:1. During the test, the atmospheric pressure (P_A) and airflow temperature (T_C) are measured at the anechoic test chamber and used to calculate the reference kinematic viscosity (ν).

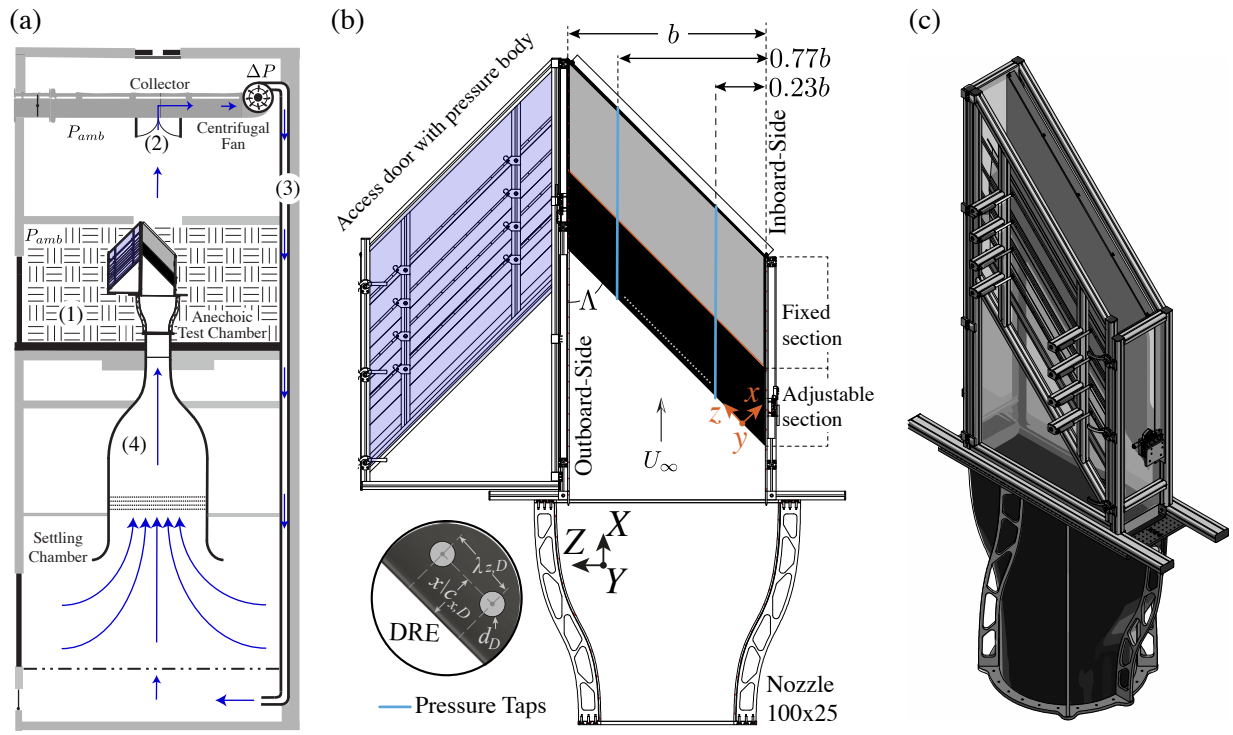

Fig. 1 Experimental Setup (note that in (a) and (b), the access door is shown in open position): (a) Cut-out diagram of the different sections of the anechoic A-tunnel with the STEP installed. (b) General schematic (flow direction bottom to top, $b \approx 0.884$ m, $c_X \approx 0.848$ m and $\Lambda \approx 45°$) of the STEP showing the adjustable (black area) fixed (gray area) flat-plate elements. (c) Isometric view of the STEP in operational conditions.

B. Swept Transition Experimental Platform

The STEP is a self-contained test section attached to the rectangular 25×100 cm^2 interchangeable nozzle. A cross-sectional schematic of the STEP is shown Fig. 1(b). Note that for visualization purposes, this schematic shows an opened access door. Instead, the operating condition (i.e., closed access door) is shown in the isometric view in Fig. 1(c) and the photograph in Fig.2(a).

The primary component of the STEP is a 20 mm thick precision machined 45-degree swept aluminum flat-plate with a modified super-elliptical (MSE) leading edge ($AR = 6$, see Schrader et al. [23]) and a flap element at the trailing edge. The flat-plate is enclosed by polycarbonate walls mounted on a custom-made aluminum frame constructed out of ITEM line 8 profiles, as shown in Fig. 1(c). Selecting optically transparent walls ensures the possibility of using non-intrusive measurement techniques (e.g., PIV, TSP).

A unique aspect of this flat-plate is that it features an adjustable leading-edge section (black element in Fig. 1b) capable of translating along the Y direction relative to the fix section (gray element in Fig. 1b) using precision micro-stages. Therefore, by changing the distance between the sections, a forward/backward facing step can be formed at their intersection (i.e., $x_h/c_x \approx 0.397$).

Figure. 1(b) shows the streamwise and orthogonal coordinate systems (i.e. X, Y, Z and x, y, z). Note that the X-direction is parallel to the test-section side wall, while the x-direction is orthogonal to the leading edge. The total reference (i.e., excluding the flap) streamwise chord is $c_X = 0.848$ m. Due to the sensitivity of CF instability to surface conditions, the leading edge is polished to a surface roughness of $R_q \approx 0.6$ µm measured using a Mitutoyo profilometer SJ-301.

Access to the measurement region is provided through a hinged door in the front part of the STEP as shown in Fig.2(b). The frame of this door supports an adjustable flexible wall which conditions the pressure distribution on the flat-plate. The shape of the wall is determined by eight independently moving linear actuators. Two rows of 63 pressure taps connected to a system of differential pressure transducers measure the flat plate's pressure distribution on the outboard and inboard section as indicated in Fig 1(b).

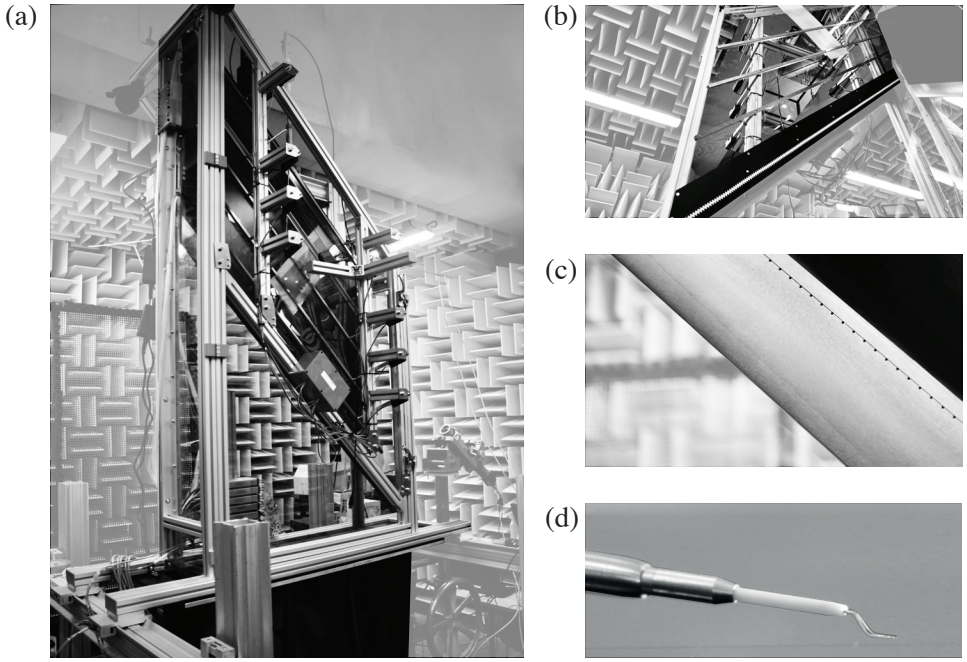

Fig. 2 Photographs of the different components of the STEP: (a) Model installed at the A-tunnel. (b) Frontal access door with adjustable pressure body. (c) Installation of DREs near the polished leading edge. (d) HWA boundary layer probe and sting during measurements.

Figure. 3(a) shows a detailed cross-sectional schematic of the intersection between the STEP and the 100×25 cm^2 nozzle. As shown in the diagram, the incoming turbulent boundary layer from the wind tunnel is bleed out at the STEP side walls to prevent leading edge contamination of the flat-plate model. The reference wind tunnel freestream velocity (U_∞) is determined using a pitot-static tube located on the STEP side wall as depicted in Fig. 3(a). The Reynolds number (Re_{c_X}) used in this study is based on U_∞ and chord length (c_X) parallel to the X direction.

Previous experiments indicate that a low turbulence environment ($Tu < 0.15\%$, see [4]) is a prerequisite for studying stationary CF instability. Figure. 3(b) shows a set of measurements of turbulence intensity (Tu) at the exit of the wind tunnel nozzle using a single wire HWA probe (Dantec 55P11). The wire sensor is parallel to the Z-axis, measuring $Tu = {}_{100/U_\infty}\sqrt{(1/2)(\overline{U'^2}+\overline{V'^2})}$. The results bandpass filtered between 2 and 5000Hz show the turbulence intensity remains low for the range $10\ \mathrm{m/s} \lesssim U_\infty \lesssim 20\ \mathrm{m/s}$.

In addition, to investigate the spanwise uniformity of the inflow at the wind tunnel operating conditions in this work ($U_\infty \approx 15$ m/s), the HWA probe located at the center of the nozzle was traversed along the Z-coordinate. The results for the time-averaged velocity (U/U_{Z0}) relative to the $Z/b = 0$ measurement and the turbulence intensity are presented in Figs. 3(c,d). Without the STEP ($\circ$ in Fig. 3d), a low turbulence intensity level is measured between $-0.33 \leq Z/b \leq 0.33$. The addition of the STEP model ($\bullet$ in Fig. 3d) on the wind tunnel nozzle leads to a subtle increase in the turbulence intensity reaching a value of $Tu \approx 0.05\%$. Based on these measurements, it is clear that the experimental facility provides acceptable flow conditions for investigating stationary CF instability.

C. Boundary-Layer Stability Analysis

Theoretical stability analysis can provide valuable insights into the amplification or decay of disturbances in a steady laminar boundary-layer solution (i.e., base flow). To do so, the instantaneous components $\mathbf{q} = \langle u, v, w, p \rangle$ are decomposed (i.e. $\mathbf{q} = \bar{\mathbf{q}} + \mathbf{q}'$) into a base flow $\bar{\mathbf{q}} = \langle \bar{u}, \bar{v}, \bar{w}, \bar{p} \rangle$ and a perturbation $\mathbf{q}' = \langle u', v', w', p' \rangle$. An overview of stability analysis methods used in the numerical/experimental study of boundary-layers prone to the development of crossflow instability can be found in [4, 24, 25].

The numerical solution of the base flow ($\bar{\mathbf{q}} = \langle \bar{u}, \bar{v}, \bar{w}, \bar{p} \rangle$) on a swept wing or flat-plate can be simplified if the spanwise invariant condition (i.e., $\partial/\partial_z = 0$ and $w_\infty = w_e = \mathrm{cst}$) is a valid assumption in the region of interest on the

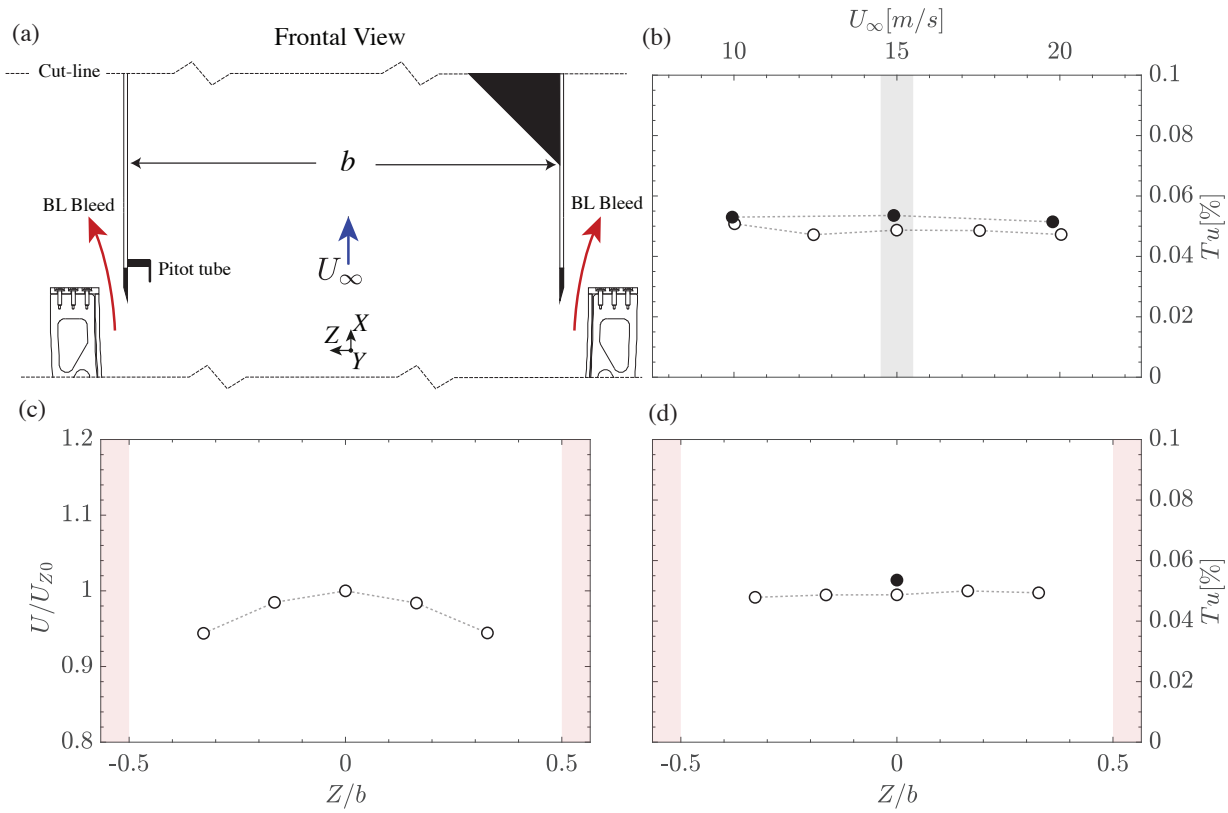

Fig. 3 Inflow characterization at the exit of the wind tunnel nozzle without ∘ and with • the STEP: (a) Cross-sectional schematic showing the nozzle junction with the STEP; (b) Turbulence Intensity (bandpass 2 Hz **$\leq f \leq$ 5000** Hz**) at different freestream velocities; (c) Spanwise uniformity of inflow velocity with reference to the measurement at $Z/b = 0$ ($U_{Z0} \approx 15$**m s^{-1}**); (d) Spanwise uniformity of Turbulence Intensity (bandpass 2** Hz **$\leq f \leq$ 5000** Hz**) for $U_\infty \approx 15$** m s^{-1} **(shaded red areas indicate bleed regions, $b \approx 0.884$** m**).**

experimental setup. If this condition applies, the 3D boundary-layer equations are reduced to a 2.5D formulation with a decoupled z-momentum equation. Considering that the no-slip and impermeability boundary conditions are enforced at the wall, the governing equations can be solved for a given external velocity distribution specified as a top boundary condition.

In experiments, the static pressure measured at the wall can be used to determine the external velocity distribution (u_e) based on the boundary-layer assumption (i.e., $\partial p/\partial y \approx 0$). In this work, u_e is determined from the experimental measurements by decomposing the free-stream velocity U_∞ into streamwise and spanwise components (i.e. u_∞ and w_∞, respectively). Then, using an logarithmic fit of the measured pressure coefficient (C_p, solid orange line in Fig.4Ic), the total velocity external to the boundary-layer is calculated as $U_e = \sqrt{(1-Cp)U_\infty^2}$. Based on the spanwise invariance condition (i.e., $w_\infty = w_e =$ cst), the local external velocity of the boundary layer is calculated as $u_e = \sqrt{U_e^2 - w_\infty^2}$.

Based on the experimental external velocity distribution $u_e(x)$, the 2.5D boundary layer equations are solved perpendicular to the leading edge (coordinate system x, y, z Fig.1b) in a Cartesian grid (without surface curvature) using a TU Delft in-house solver. The solver employs a marching method initiated using a Falkner-Skan-Cooke solution [see 26]. The discretization in the streamwise direction follows second-order backward Euler (implicit) finite differences, while a Chebyshev spectral collocation method is used for the wall-normal direction [see 27, 28, Ch.3].

The stability of the base flow is calculated using a TU Delft in-house code [29] which solves the Linear Parabolized Stability Equations (LPSE) [see 30] in the spatial theory formulation ($\omega = \omega_r$, $\alpha = \alpha_r + \alpha_i$ and $\beta = \beta_r + \beta_i$). The corresponding ansatz is given by Eq. 1.

$$q'(x, y, z, t) = \phi_q(x, y) e^{i\left(\int_{x_0}^{x} \alpha(x)dx + \beta z - \omega t\right)} + c.c. \tag{1}$$

The assumption of spanwise invariant laminar base flow implies that instabilities can only grow in the streamwise direction (i.e. $\beta_i = 0$). Thus, considering stationary CF instability modes ($\omega = 0$), amplification N-factor curves are calculated by integrating the spatial streamwise growth rate α_i along the x coordinate for a fixed spanwise wavenumber ($\beta_r = 2\pi/\lambda_z$). Finally, an important remark is that near the late stages of amplification of the CF modes and before transition, a linear stability analysis is not valid [see 30].

D. Measurement Technique and Flow Metrics

The boundary layer flow was measured using a Dantec 55P15 Hot-Wire Anemometer (HWA) probe connected to a constant temperature bridge (TSI IFA-300). An analog-digital (24-bit) acquisition system records the voltage signal of the HWA. Then, based on the methodology described by [31] an in-situ calibration, including temperature and atmospheric pressure corrections, is used to determine the flow velocity from the HWA voltage signal.

A custom stainless steel sting connected to an automated traversing system (Fig. 2d) on the STEP frame allows for the precise movement (i.e., step accuracy of ±6.2 µm) of the HWA probe in the X, Y, Z axis. Inevitable mechanical vibrations in the sting are monitored using a three-axial accelerometer (Analogue Devices ADXL335) to identify the characteristic resonant frequencies of the system.

The single wire sensor is horizontal (i.e., parallel to the Z axis) and orthogonal to the X axis. Note that as indicated by Rius-Vidales and Kotsonis [32], the velocity measured by the HWA in this orientation can be simplified as the Euclidean sum: $Q = \sqrt{(u\cos\Lambda + w\sin\Lambda)^2 + v^2}$. The streamwise development of the boundary layer is captured through several wall-normal boundary-layer scans (y-z measurement planes) between $0.3 < x/c_x < 0.9$. Each scan consists of 35×55 measurement points at which the HWA signal is acquired for 2 seconds at a sampling frequency of $f_s = 51200$ Hz. The resolution along the span is fixed to $\Delta z \approx 555$ µm while the wall-normal one is logarithmically distributed towards the wall.

During post-processing, a linear regression was performed on the velocity profiles to retrieve the wall location. Then, following the methodology outlined [7, 33] the steady disturbance profile $\langle \hat{q}(y) \rangle_z$ is calculated using Eq. 2 for each measurement plane. In this work, the non-dimensional maximum of these profiles ($A_M = \max(\langle \hat{q}(y) \rangle_z)/\bar{Q}_e$) is used as a metric to monitor changes in the primary CF instability.

$$\langle \hat{q}(y) \rangle_z = \sqrt{\frac{1}{n} \sum_{j=1}^{n} (\bar{Q}(y, z_j) - \bar{Q}_z(y))^2} \tag{2}$$

To analyze the unsteady disturbances, the methodology used in [6, 7, 33] and described by Eq.3 is followed. That is, for each y-z measurement plane, a profile in the wall-normal direction is calculated through a numerical integration along the z axis of the temporal standard deviation (σ_Q) at every y position. Then, a second integration follows along the y-axis to obtain the amplitude a, which is used as a metric to evaluate the streamwise development of the secondary CF instability.

$$a = \frac{1}{\bar{Q}_e} \frac{1}{y^m} \frac{1}{z^m} \int_0^{y^m} \int_0^{z^m} \sigma_Q(y, z) dz dy \tag{3}$$

III. Results

The main objective of the STEP is to generate the experimental conditions required for the detailed study of the interaction of surface irregularities and the effects of LFC techniques on the development of primary and secondary CF instability. As described by Saric et al. [5], different instabilities can dominate the laminar-turbulent transition in three-dimensional boundary layers. These are attachment line contamination/instabilities, Görtler Vortices, Tollmien-Schlichting waves, and CF instability. Fortunately, by bleeding out the turbulent wind tunnel boundary-layer on the side walls, the small radius of the MSE leading edge, and the lack of concave surface curvature (i.e., flat-plate model), the boundary-layer flow is only then susceptible to the development of either TS waves or CF instability. Thus, a high sweep angle (45°) and a pressure distribution with a favorable pressure gradient are enforced on the flat-plate to ensure that CF instability dominates the STEP laminar-turbulent transition.

Enforcing a target pressure distribution on the STEP is possible, given that the model offers the capability of simultaneously modifying the shape of the pressure wall while recording the resulting pressure distribution on the flat-plate during wind tunnel operation. The measured pressure distribution is shown in Fig. 4(Ic) for the conditions of this work at $Re_{c_X} \approx 8.6 \times 10^5$ ($U_\infty \approx 15$ m s^{-1}). An important characteristic shown in Fig. 4(Ic) is the nearly identical trend and small differences in the outboard and inboard pressure measurements. This match indicates that the spanwise invariant condition (i.e., infinite swept wing) is a valid assumption in the boundary-layer stability analysis of this experimental setup.

Following the methodology described in Sec.II.C, the boundary-layer flow (i.e. baseflow) was calculated using the logarithmic fit of the measured pressure distributions of the STEP given by the orange solid line in Fig.4(Ic). Then, boundary-layer stability was assessed through the Linear Parabolized Stability Equations (LPSE). The LPSE results reveal that a stationary CF mode featuring a spanwise wavelength of $\lambda_{z,D} \approx 10$mm is highly unstable at the conditions under study and would monotonically grow in the measurement region.

In line with previous experimental work on the fundamental study of primary and secondary CF instability [e.g. 6, 7, 34] cylindrical Discrete Roughness Elements (DREs) are positioned near the leading edge (Fig.2c) to condition the amplitude and wavelength of the stationary CF instability. The DREs are manufactured in-house from an adhesive vinyl film cut to specifications using a CNC cutting machine. The DREs are spaced at $\lambda_{z,D} \approx 10$ mm. Table.1, shows the parameters of the forcing cases under study. As the HWA measurement will show, the unequal DREs height between cases A and B leads to noticeable differences in the streamwise development of the CF vortices at the measurement region.

A. Development of Stationary Disturbances

Figure. 4(Ia-IIb) presents selected spanwise-averaged mean flow boundary-layer profiles ($\bar{Q}_z$) for all cases in Table.1. The displacement thickness ($\delta^*_Q \approx 634$ µm at $x/c_x \approx 0.3$) at the first measurement plane is used to non-dimensionalize the wall-normal y coordinate. Considering first the most upstream measurements (Fig.4Ia), the mean flow distortion exerted due to the development of the CF vortices is unnoticeable. In both forcing conditions (A) and (B), the boundary layer profiles closely match the one dictated by the numerical boundary-layer solution (BLS). This trend continues until $x/c_x \approx 0.6$, where clear deviations become noticeable in case B (Fig. 4Ib), which feature the DREs with the highest relative height. Figure 4(IIc) shows the streamwise evolution of the integral parameters under different forcing conditions.

As explained in Sec.I, the primary CF instability manifests as a series of co-rotating vortices in the boundary layer. Depending on a combination of the turbulence level and surface roughness, this crossflow (CF) vortices can either travel along the span or remain fixed to the surface [see 4, 5]. In experiments, a good indication of which of the two is dominant can be inferred from the transition front pattern obtained using optical (e.g. IR or TSP) or surface (e.g. napthalene or oilflow) visualizations. A smeared pattern along the span indicates the dominance of traveling CF instability. Instead, a jagged or saw-tooth pattern indicates the dominance of stationary CF instability modes over

Case	$\bar{h}$	T_w/T_0	$\lambda_{z,D}$ mm	d_D mm	k_D µm	s_D/c_x
A	-	≈ 1	10	2	70	0.1
B	-	≈ 1	10	2	125	0.1

Table 1 Forcing conditions of tested configurations at $Re_{cX} \approx 8.6 \times 10^5$ and flap angle of ≈ 18 °

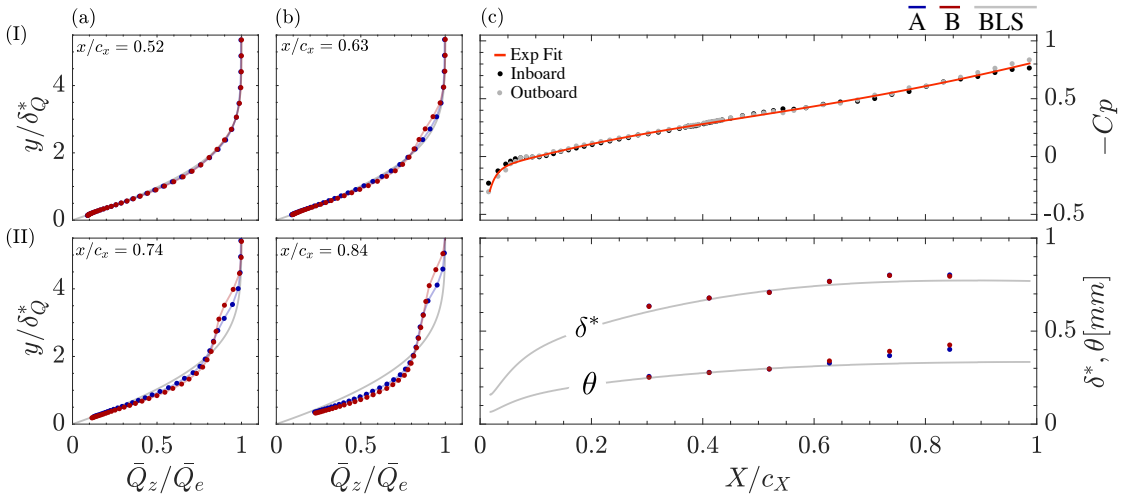

Fig. 4 Boundary Layer development for case A (red), case B (blue) and numerical boundary-layer solution (BLS, gray): (Ia-IIb) Selected boundary layer profiles of spanwise averaged mean flow velocity $\bar{Q}_z$. (Ic) Measured pressure distribution over the flat-plate element. (IIc) Integral boundary layer properties ($\delta^*_Q \approx 634$µm).

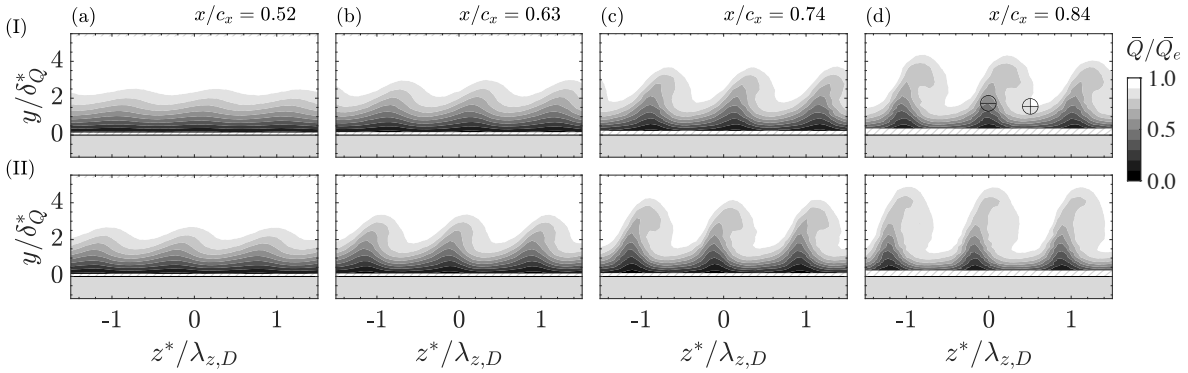

Fig. 5 Contours of time-average velocity (z positive direction outboard) at different streamwise locations: (I) Case A; (II) Case B ($\delta^*_Q \approx 634$ µm and $\lambda_{z,D} \approx 10$ mm)

traveling ones. Even though it is planned to incorporate optical boundary-layer diagnostics Temperature Sensitive Paint (TSP) on the STEP, at the moment, only conclusions drawn from the HWA information are possible.

As the crossflow instability develops, the ensuing co-rotating CF vortices lead to a spanwise modulation of the boundary layer flow. The direct consequence of the CF vortices is the transport of high-momentum fluid from the edge of the boundary layer towards the wall (downwelling region, ⊕ in Fig. 5Id) and low momentum (upwelling region ⊖ in Fig. 5Id) one from the wall towards the edge of the boundary layer. The time-averaged velocity contours ($\bar{Q}$) at different streamwise locations in Fig. 5 show this distortion on the boundary-layer flow. Given that each HWA point-wise measurement is uncorrelated in time, the time-average boundary-layer topology indicates the dominance of stationary CF instability modes over traveling ones. Thus, by combining the STEP and the wind tunnel facility, the necessary conditions for the fundamental study of stationary CF instability are met.

In addition, a detailed inspection of the topology of the velocity fields presented in Fig. 5 reveals that the selected CF instability mode forced by the DREs based on the LPSE stability analysis was an adequate choice. The selected CF instability mode (i.e. $\lambda_{z,D} \approx 10$ mm) is highly unstable at the conditions of this study since the wavelength of the

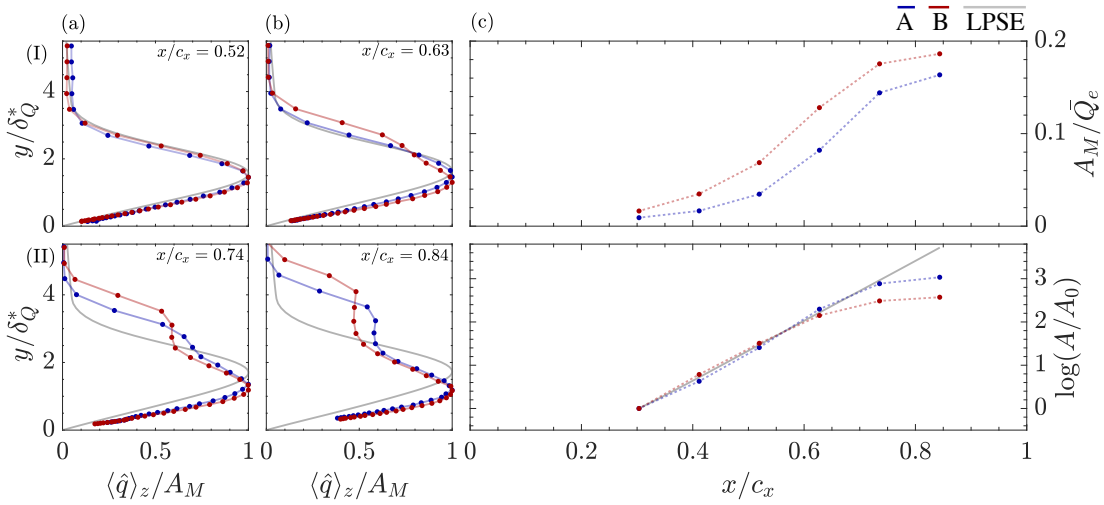

Fig. 6 Primary CF instability development: (Ia-IIb) Selected steady disturbance $\langle\hat{q}\rangle_z$ profiles ($\delta^*_Q \approx 634$ µm). (Ic) Streamwise development of the non-dimensional maximum amplitude (A_M). (IIc) Comparison of HWA measurement growth of the steady disturbance to linear PSE stability calculations.

vortices matches the spanwise spacing of DREs (i.e., $z/\lambda_{z,D} \approx 1$) in all measurement locations.

Following the methodology described in Sec.II.D The steady disturbance profile $\langle\hat{q}\rangle_z$ has been calculated from the time-averaged velocity fields ($\bar{Q}$) at each measurement plane to assess the development of the primary CF instability. For selected positions, the resulting profiles are presented in Fig. 6(Ia-IIb), and their maximum amplitude (A_M) extracted at each measurement location and presented in Fig. 6(Ic).

Analyzing the shape of these profiles reveals essential aspects of the regime of amplification of the CF instability. For upstream stations (Fig. 6Ia) the profiles only display one distinguishable lobe, which is suggestive that the CF vortices are in their linear stage. Figure 6(IIc), shows a comparison of the amplification curve from the LPSE stability analysis to the one calculated from HWA measurements. A nearly perfect match between the shape and growth rate of the instabilities up to $x/c_x \approx 0.6$ is observed. This comparison formally confirms that the amplification of the instability is in the linear stage for a large streamwise portion of the flat-plate.

As the crossflow vortices develop downstream of $x/c_x \approx 0.6$, they enter a non-linear amplification stage where the interaction between the primary CF instability and its harmonics eventually leads to their saturation as the boundary layer flow reaches its strongest spanwise modulation. From this point onwards, high-frequency secondary instabilities emerge on the strong shear layer region at the side (i.e., outer upwelling region) and top of the vortices. The creation of a second lobe (Fig. 6IIa-IIb)is characteristic of the non-linear stages of the CF instability development [see 7, 30] and an amplitude saturation of the primary instability occurs as shown in Fig. 6IIc. It is interesting to note that the amplitude saturation level is in agreement with the values collected by Downs and White [33, figure 19] for different studies on 45-degree swept models in different wind tunnels under similar low turbulence environments.

Up to this point, it is clear that the STEP can reproduce the necessary experimental conditions to allow for the detailed study of the linear and non-linear stages of the development of CF instability. In the following section, a rigorous study of the development of secondary CF instability using frequency analysis and spectral filtering of the velocity measurements will be presented.

B. Development of Unsteady Disturbances

This section presents a detailed analysis of unsteady disturbances interacting with the primary CF instability. Coherent velocity fluctuations at specific locations within the stationary CF vortices structure have been associated with unsteady modes of different natures. Based on the current understanding [e.g. 8, 35–37], type III modes are related to the interaction between stationary and traveling primary CF instability modes and manifest on the upwelling region

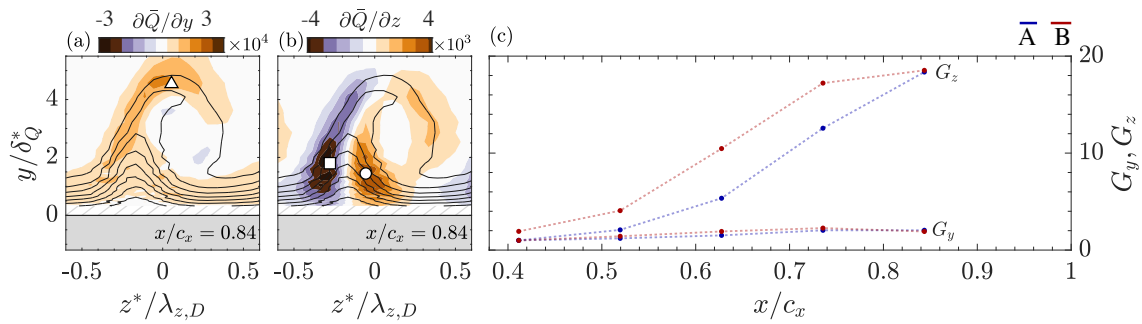

Fig. 7 Contours of time-averaged wall-normal (a) and spanwise (b) velocity gradients indicating the extraction of spectral probes (P_1 □,P_2 △, and P_3 ○) and time-averaged velocity (black solid line 10 levels $\bar{Q}/\bar{Q}_e$ as in Fig. 5) at $x/c_x \approx 0.84$. Streamwise development (c) of the minimum spanwise (G_z) and maximum wall-normal (G_y) gradients. See text for the definition of G_z and G_y. ($\delta^*_Q \approx 634$ µm and $\lambda_{z,D} \approx 10$ mm)

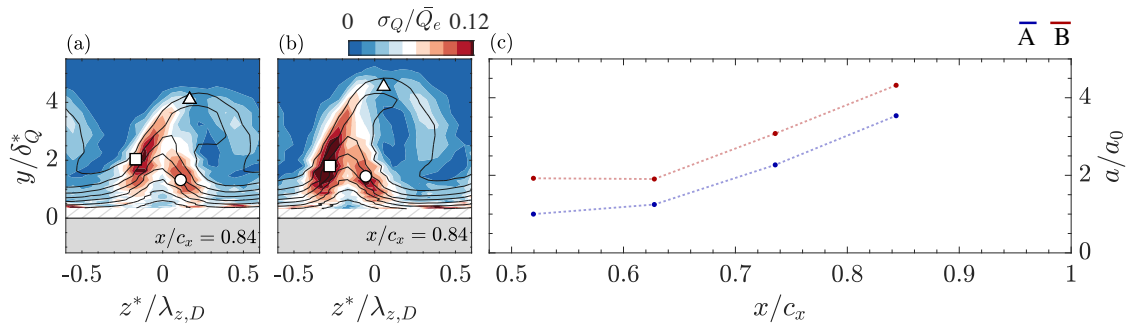

Fig. 8 Contours of total temporal velocity fluctuations indicating the extraction of spectral probes (P_1 □,P_2 △ and P_3 ○) and time-averaged velocity (black solid line 10 levels $\bar{Q}/\bar{Q}_e$ as in Fig. 5) at $x/c_x \approx 0.84$: (a) Case A; (b) Case B; and (c) Streamwise development of the total unsteady disturbance amplitude (a) with a_0 corresponding to the value for case A at $x/c_x \approx 0.52$ ($\delta^*_Q \approx 634$ µm and $\lambda_{z,D} \approx 10$ mm).

inner-side (regions of $\partial/\partial z > 0$, ○ in Fig.7b). In contrast, type I and II modes are related to secondary inviscid shear layer instabilities which manifest on the outer side (regions of $\partial/\partial z < 0$, □ in Fig.7b) and top of the CF vortices (regions of $\partial/\partial y > 0$, △ in Fig.7a).

The development of secondary CF instabilities is constrained to the non-linear stages of the primary instability development, given that they originate from the strong shear regions of the distorted boundary-layer flow. Soon after their onset, they rapidly amplify and lead to the breakdown of the CF vortices and transition [see 6, 7, 17].

To monitor streamwise changes in the time-averaged velocity spanwise and wall-normal gradients, the local minima/maxima velocity gradients pertaining to the CF vortex at the mid-measurement domain are extracted at each measurement plane. Figure.7(c) shows the results for the spanwise gradient $G_z = \min(\partial\bar{Q}/\partial z)/\min(\partial\bar{Q}_0/\partial z)$ and for the wall-normal $G_y = \max(\partial\bar{Q}/\partial y)/\max(\partial\bar{Q}_0/\partial y)$. Note that the reference values $\min(\partial\bar{Q}_0/\partial z)$ and $\max(\partial\bar{Q}_0/\partial y)$ correspond to the ones extracted from the lower forcing case A at $x/c_x \approx 0.42$.

Changes in the negative spanwise and positive wall-normal gradients are relevant for the evolution of type-I and II modes. Analyzing the higher amplitude forcing case B in Fig.7(c) shows that the gradual linear amplification of the CF vortices correlates well with the presence of stronger velocity shears. The strongest velocity shears occur as the CF vortices reach amplitude saturation at the non-linear stage ($x/c_x > 0.6$). The overall change in the spanwise and wall-normal gradients correlates well with the increase of the total unsteady disturbance amplitude (a/a_0) presented in Fig. 8(c). Note that here also a_0 is based on the unsteady disturbance amplitude from the lower forcing case A at $x/c_x \approx 0.52$.

Contours of total temporal velocity fluctuations (σ_Q) for the measurement plane $x/c_x \approx 0.84$ are shown in Fig.8(a,b).

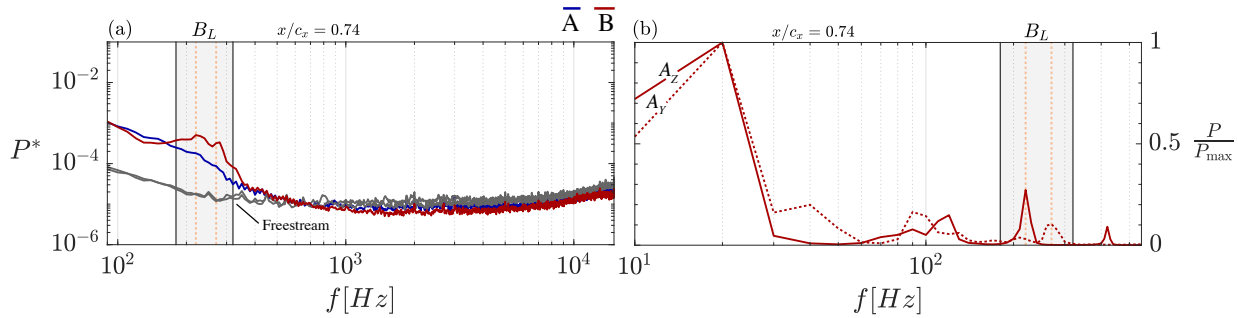

Fig. 9 Spectral analysis of probe P_3 (∘ in Fig. 8) velocity fluctuation (a) and accelerometer signal (b) located at the upwelling region inner-side at $x/c_x \approx 0.74$. Shaded gray region indicate the frequency bands and the dashed orange lines indicate mechanical vibrations of the HWA sting.

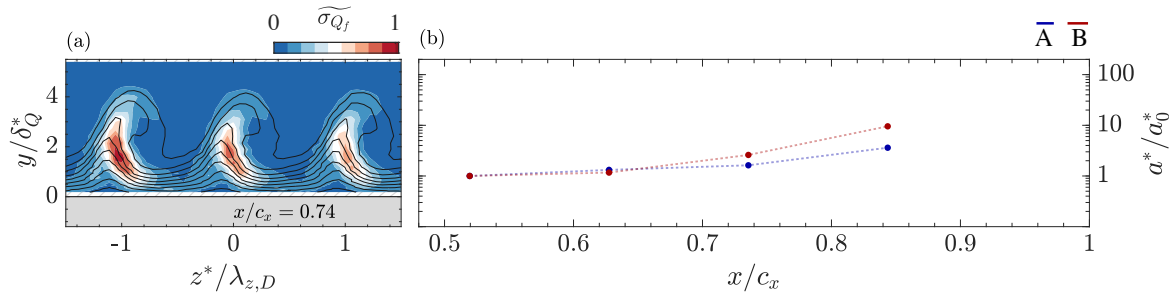

Fig. 10 Bandpass filtered (B_{H1}, 180 Hz $\lesssim f \lesssim$ 320 Hz) velocity fluctuation: (a) Contours and time-averaged velocity (black solid line 10 levels $\bar{Q}/\bar{Q}_e$ as in Fig.5IIc) at $x/c_x \approx 0.74$; (b) Streamwise development of the filterted unsteady disturbance amplitude (a^*). ($\delta^*_Q \approx 634$ µm and $\lambda_{z,D} \approx 10$ mm)

As expected, temporal velocity fluctuations (σ_Q) occur at specific locations within the stationary CF vortices structure. Namely, at the inner/outer side of the upwelling region and the top of the crossflow vortices. To classify these velocity fluctuations and associate them to unsteady modes of type I, II or III, the HWA time series is extracted at three spatial probe locations (P_1 □,P_2 △ and P_3 ∘) as indicated in Fig. 8(a,b) for the two cases A and B. Then, a spectral analysis using the averaged periodogram method by Welch [38] is applied to each probe signal. The final power spectral density (P) curves presented in Figs. 9 and 11 feature a frequency resolution of $\delta_f = 10$ Hz (segments of 5120 samples and overlap of 50%). Following Deyhle and Bippes [39], the spectra is non-dimensionalized as: $P^* = ((\delta_f P)/U_\infty^2)^{1/2}$.

In addition, following Serpieri and Kotsonis [6, 40] a zero-phase eighth-order Butterworth filter has been used to filter the velocity fields at particular frequency bands. Then, by calculating the temporal standard deviation (σ_{Q_f}), the topology of the velocity fluctuations at each frequency band can be analyzed. Note that the velocity fluctuations ($\widetilde{\sigma_{Q_f}} = \sigma_{Q_f}/\max(\sigma_{Q_f})$) are referenced to the filtered maximum fluctuations at each measurement plane.

1. Stationary and traveling crossflow modes interaction

The nonlinear interaction between stationary and traveling CF modes can be identified through the analysis of coherent velocity fluctuations in the regions type III modes [see 6, 7]. That is on the inner-side of the CF vortices, at regions of positive spanwise gradient ($\partial\bar{Q}/\partial z > 0$) and at the location of probe P_3 (∘ in Fig. 8a,b).

The spectral analysis of the velocity fluctuations related to probe P_3 are presented in Fig.9(a) for the measurement plane $x/c_x \approx 0.74$ and two cases, A and B. The frequency content at the freestream reference probe (i.e., solid gray line) is relatively flat compared to the ones inside the boundary layer at P_3 location. The spectra for case B reveal the dominance of velocity fluctuations inside a low-frequency band (B_L) between 180 Hz $\lesssim f \lesssim$ 320 Hz.

A detailed inspection of the spectra at this frequency band reveals two low-frequency peaks at $f \approx 220$ and 270 Hz (dashed orange lines in Fig.9a). An spectral analysis of the accelerometer signals which record the spanwise (A_Z)

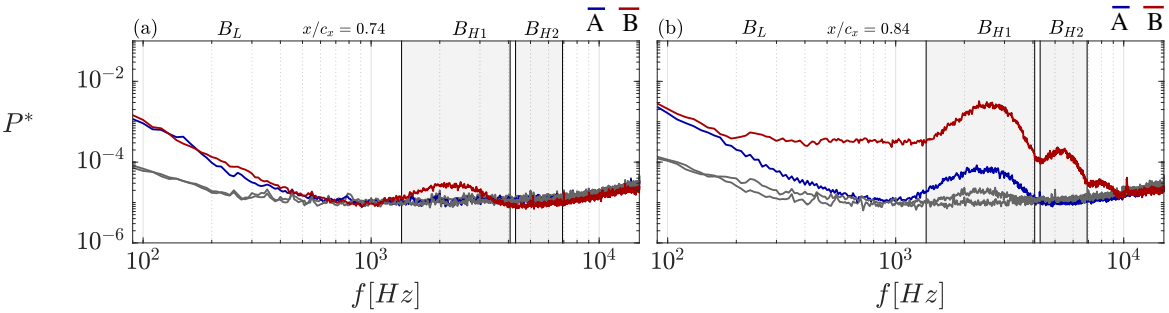

Fig. 11 Spectral analysis of probe P_1 (□ in Fig. 8) located at the outer-side of the upwelling region: (a) $x/c_x \approx 0.74$; and (b) $x/c_x \approx 0.84$. Shaded gray region indicate the frequency bands and the dashed orange lines the mechanical vibrations of the HWA sting based on Fig.10

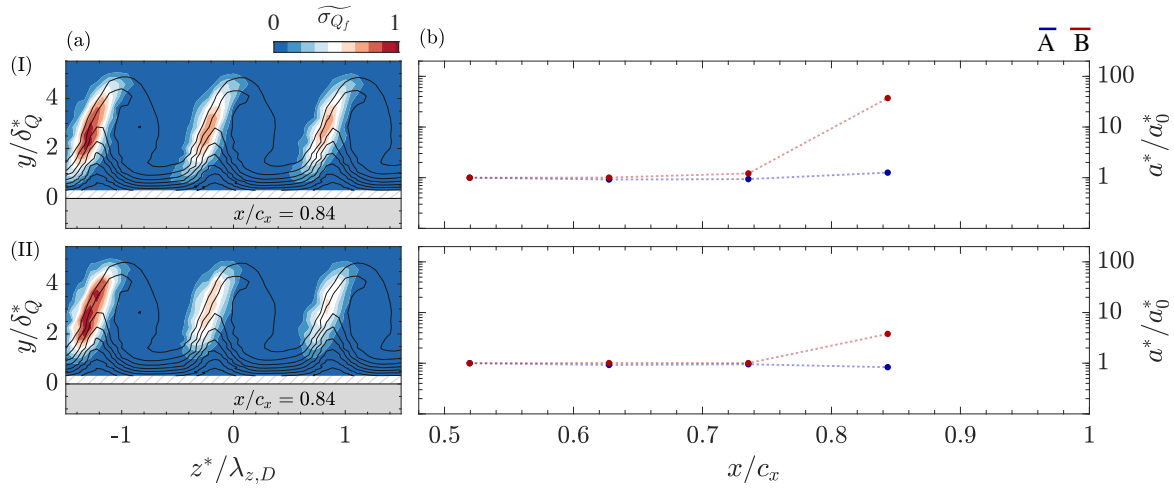

Fig. 12 Bandpass filtered (I, B_{H1}, 1.4 kHz $\lesssim f \lesssim$ 4.1 kHz and II, B_{H2}, 4.3 kHz $\lesssim f \lesssim$ 6.9 kHz) velocity fluctuations: (a) Contours and time-averaged velocity (black solid line 10 levels $\bar{Q}/\bar{Q}_e$) at $x/c_x \approx 0.84$; (b) Streamwise development of the filterted unsteady disturbance amplitude (a^*). ($\delta_Q^* \approx 634$ µm and $\lambda_{z,D} \approx 10$ mm)

and wall-normal (A_Y) vibrations at the location of probe P_3 were performed to investigate this further. The results in Fig.9(b) show that most vibrations occur at low frequencies and confirm that the identified frequency peaks in band B_L are related to unavoidable mechanical vibrations from the HWA sting structure.

Contours of filtered temporal velocity fluctuations in Fig.10 show that they occur on the inner-side of the CF vortices and overlap with regions of positive spanwise gradients (see Fig.7b). In agreement with [6, 7], the low-frequency content and topology of the velocity fluctuations suggest a relation to type-III mode.

The development of the unsteady disturbance amplitude for this frequency band (a^*) is shown in Fig.10(c). Note that here also a_0^* is based on the unsteady disturbance amplitude for each case at $x/c_x \approx 0.52$. The results show a gradual amplification of the velocity fluctuations related to type-III, especially downstream of $x/c_x > 0.6$. This behavior indicates that, in addition to stationary CF modes, traveling modes in the frequency range of B_L are destabilized in the measurement region. Nevertheless, as previously discussed, the time-average boundary layer topology indicates the dominance of stationary CF instability modes over traveling ones.

2. Secondary instabilities and breakdown of the crossflow vortices

In experiments, the development of secondary CF instability is studied by analyzing temporal velocity fluctuations in regions pertaining to type I and II modes. That is on the outer-side and top of the CF vortices, at regions overlapping

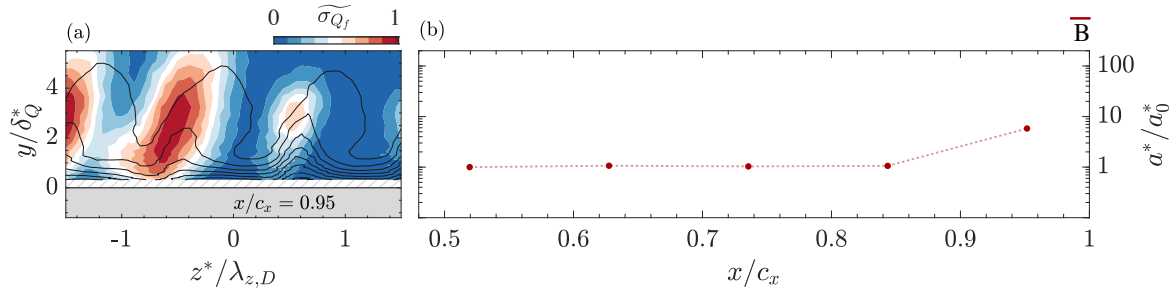

Fig. 13 Highpass filtered ($f \geq 12$ kHz) velocity fluctuation: (a) Contours and time-averaged velocity (black solid line 10 levels $\bar{Q}/\bar{Q}_e$ as in Fig.5) at $x/c_x \approx 0.95$; (b) Streamwise evolution of the filterted unsteady disturbance amplitude (a^*). ($\delta^*_Q \approx 634$ µm and $\lambda_{z,D} \approx 10$ mm)

with negative spanwise ($\partial\bar{Q}/\partial z < 0$) and positive wall-normal ($\partial\bar{Q}/\partial y > 0$) gradients. In this work, two probes P_1 and P_2 (□ and △ in Fig.8a,b) are used to identify the frequency of type-I and type-II modes, respectively.

A spectral analysis of the velocity fluctuations related to probe P_1 is presented in Fig.11(a,b) for the measurement plane $x/c_x \approx 0.74$ and $x/c_x \approx 0.84$. The spectra show high-frequency temporal velocity fluctuations that intensify as the initial amplitude of the CF vortices increases (i.e., comparing cases A and B). Based on these observations, two high-frequency bands of interest are identified: B_{H1} (1.4 kHz $\lesssim f \lesssim$ 4.1 kHz) and B_{H2} (4.3 kHz $\lesssim f \lesssim$ 6.9kHz).

Figure.12(Ia,IIa) present the bandpass filtered temporal velocity fluctuations ($\widetilde{\sigma_{Q_f}}$) based on the identified frequency bands B_{H1} and B_{H2}. The $\widetilde{\sigma_{Q_f}}$ contours reveal that the fluctuations concentrate at the upwelling region outer-side and overlap with the negative spanwise gradients shown in Fig.7(b). The high-frequency content and the topology of these temporal velocity fluctuations are in agreement with a type-I secondary CF instability [see 6, 7, 40].

Detailed numerical investigations by Bonfigli and Kloker [8] have shown that type-I modes are related to high-frequency secondary instabilities of Kelvin-Helmholtz type. Their amplification and onset are directly influenced by the spanwise modulation of the boundary-layer flow as they develop on the shear layer on the upwelling region outer side of the stationary CF vortices and manifest as a secondary set of finger-vortices [see 6, 36]. Henceforth, their frequency varies as they convect along the shear layer. This frequency change can be clearly observed when comparing Fig.12(Ia) with Fig.12(IIa), as the fluctuations for the frequency band B_{H1} are slightly closer to the wall than the ones for the band B_{H2}.

Figures.12(Ib-IIb) shows the streamwise development of the unsteady disturbance amplitude for frequency bands B_{H1} and B_{H2}. The results show that as the stationary CF vortices saturate ($0.74 \lesssim x/c_x \lesssim 0.84$ in Fig. 6IIc), type-I secondary CF instabilities rapidly amplify. This behavior is not unexpected, as it has been previously observed that their rapid amplification leads to the breakdown of the CF vortices and the laminar-turbulent transition [6, 7]. In fact, the spectra close to this location (i.e. $x/c_x \approx 0.84$ Fig.11b) reveal a considerable uniform increase of fluctuations at low frequencies, which could signal a potential start of the laminar-turbulent transition process. Henceforth, to adequately characterize the breakdown of the CF vortices in the higher amplitude case B, an extra measurement plane at $x/c_x \approx 0.95$ was performed. Fig.13(a), shows the temporal velocity fluctuations after applying a high-pass filter ($f_c \geq 12$ kHz) to separate the fluctuations associated with turbulent flow from the ones related to the secondary CF instability. As expected, the breakdown of the CF vortices originates from the region where type-I secondary CF instability modes have been identified. Moreover, by applying a high-pass filter on the remaining planes of case B and calculating the unsteady disturbance amplitude, Fig.13(b) show that the turbulent fluctuations only occur for $x/c_x > 0.84$. That is after the primary CF instability reaches saturation and the type-I secondary CF instability has rapidly amplified.

Lastly, regarding the identification of type-II modes, the spectral analysis (not shown) of probe P_2 (△ in Fig.8a,b) return similar frequency bands as the ones identified with probe P_1. Therefore, it is possible that in the STEP, the type-II instability does not have a significant role in the breakdown of the CF vortices. To clarify this, numerical secondary stability analysis such as those conducted by Groot et al. [41] on a swept wing would be valuable for identifying the frequencies and regions of possible development.

Overall, the results presented in this section show that the development of stationary primary CF instability in the STEP model creates the conditions for a type-I secondary CF instability. In addition, it is also determined that prior to the laminar-turbulent transition a rapid amplification of this secondary CF instability occurs.

IV. Concluding Remarks

Controlling the laminar-turbulent boundary layer transition in high-subsonic aircraft is a topic of particular interest in the quest to reduce the environmental impact of civil aviation. A laminar flow control strategy aims to limit the growth of instabilities in the laminar boundary layer to delay its transition to turbulence and reduce the aircraft's skin-friction drag component. Relevant to swept wings is the so-called crossflow instability, which develops as co-rotating vortices in the laminar boundary layer.

The fundamental study of the interaction of crossflow instability with surface irregularities (e.g., steps and gaps) and changes in surface temperature (e.g., heating vs cooling) is paramount for designing novel control strategies. Thus, a Swept Transition Experimental Platform (STEP) has been designed and tested to expand the existing research capabilities on laminar flow control at TU Delft. The STEP is a self-contained model fully instrumented, which features a 45-degree swept flat plate, an adjustable pressure body, and an integrated HWA traverse system. The advantage of the STEP over other existing swept wing models is the flexibility in adjusting the imposed pressure distribution, full optical access capability, and modularity for simulation of surface irregularities and integration of flow control devices.

The experiments presented in this work show that the combination of the STEP and the low-turbulence environment of the TU Delft A-tunnel are sufficient for the detailed study of the development of the primary and secondary crossflow instability. Static pressure measurements at the wall on the plate's outboard and inboard side indicate that the spanwise invariant condition is a valid assumption in the measurement region of this experimental setup. The initial amplitude and wavelength of the primary stationary crossflow instability are conditioned using discrete roughness elements. In addition, through hot-wire boundary-layer scans, the linear and non-linear development stages of the primary crossflow instability are characterized. At the linear stage, a stability analysis based on the Linear Parabolized Stability Equations shows good agreement with the hot-wire measurements.

In the non-linear stage, the development of unsteady perturbations is evident in the velocity measurements. Low and high-frequency temporal velocity fluctuations are identified. Based on the frequency content and spatial organization, the low-frequency perturbations are associated with the interaction between the dominant stationary and unstable traveling crossflow modes. Instead, the high-frequency perturbations are identified as secondary crossflow instability modes that develop on the shear layer on the outer side of the upwelling region of the stationary crossflow vortices structure. As the primary instability saturates, the temporal velocity fluctuations in this region rapidly intensify, and the breakdown of the crossflow vortices is observed shortly downstream.

Overall, the STEP offers the possibility of studying the development and control of crossflow instability. The authors envision extensively using this platform to provide valuable knowledge for designing future laminar flow components.

Acknowledgments

The authors would like to acknowledge our colleagues T. van de Weijer, N. Rajendakumar, and S. Westerbeek for their support during the experiments, boundary layer stability calculations, and fruitful discussions in the analysis of the results. In addition, technical support provided by S. Bernardy, E. Langedijk and J.M. Looman is greatly appreciated. This project has been conducted under the financial contribution of the European Research Council through Starting Grant 803082 "GLOWING".

References

[1] Joslin, R. D., "Aircraft Laminar Flow Control," *Annual Review of Fluid Mechanics*, Vol. 30, No. 1, 1998, pp. 1–29. https://doi.org/10.1146/annurev.fluid.30.1.1.

[2] Schrauf, G., "Status and perspectives of laminar flow," *The Aeronautical Journal (1968)*, Vol. 109, No. 1102, 2005, pp. 639–644. https://doi.org/10.1017/S000192400000097X.

[3] Saric, W., Carpenter, A., and Reed, H., "Passive control of transition in three-dimensional boundary layers, with emphasis on discrete roughness elements," *Philosophical Transactions of the Royal Society A: Mathematical, Physical and Engineering Sciences*, Vol. 369, No. 1940, 2011, pp. 1352–1364. https://doi.org/10.1098/rsta.2010.0368.

[4] Bippes, H., "Basic experiments on transition in three-dimensional boundary layers dominated by crossflow instability," *Progress in Aerospace Sciences*, Vol. 35, No. 4, 1999, pp. 363 – 412. https://doi.org/https://doi.org/10.1016/S0376-0421(99)00002-0.

[5] Saric, W. S., Reed, H. L., and White, E. B., "Stability and Transition of Three-Dimensional Boundary Layers," *Annual Review of Fluid Mechanics*, Vol. 35, No. 1, 2003, pp. 413–440. https://doi.org/10.1146/annurev.fluid.35.101101.161045.

[6] Serpieri, J., and Kotsonis, M., "Three-dimensional organisation of primary and secondary crossflow instability," *Journal of Fluid Mechanics*, Vol. 799, 2016, pp. 200–245. https://doi.org/10.1017/jfm.2016.379.

[7] White, E. B., and Saric, W. S., "Secondary instability of crossflow vortices," *Journal of Fluid Mechanics*, Vol. 525, 2005, pp. 275–308. https://doi.org/10.1017/S002211200400268X.

[8] Bonfigli, G., and Kloker, M., "Secondary instability of crossflow vortices: validation of the stability theory by direct numerical simulation," *Journal of Fluid Mechanics*, Vol. 583, 2007, pp. 229–272. https://doi.org/10.1017/S0022112007006179.

[9] Saric, W. S., West, D. E., Tufts, M. W., and Reed, H. L., "Experiments on Discrete Roughness Element Technology for Swept-Wing Laminar Flow Control," *AIAA Journal*, Vol. 57, No. 2, 2019, pp. 641–654. https://doi.org/10.2514/1.J056897.

[10] Borodulin, V. I., Ivanov, A. V., Kachanov, Y. S., Mischenko, D. A., Örlü, R., Hanifi, A., and Hein, S., "Experimental and theoretical study of swept-wing boundary-layer instabilities. Unsteady crossflow instability," *Physics of Fluids*, Vol. 31, No. 6, 2019, p. 064101. https://doi.org/10.1063/1.5094609.

[11] Lemarechal, J., Costantini, M., Klein, C., Kloker, M., Würz, W., Kurz, H., Streit, T., and Schaber, S., "Investigation of stationary-crossflow-instability induced transition with the temperature-sensitive paint method," *Experimental Thermal and Fluid Science*, Vol. 109, 2019, p. 109848. https://doi.org/10.1016/j.expthermflusci.2019.109848.

[12] Saeed, T. I., Mughal, M. S., and Morrison, J., "The Interaction of a Swept-Wing Boundary Layer with Surface Excrescences," *54th AIAA Aerospace Sciences Meeting*, 2016, pp. AIAA Paper 2016–2065. https://doi.org/10.2514/6.2016-2065.

[13] Arnal, D., Gasparian, G., and Salinas, H., "Recent advances in theoretical methods for laminar-turbulent transition prediction," *36th AIAA Aerospace Sciences Meeting and Exhibit*, 1998. https://doi.org/10.2514/6.1998-223, aIAA Paper 1998-223.

[14] Eppink, J. L., "Mechanisms of stationary cross-flow instability growth and breakdown induced by forward-facing steps," *Journal of Fluid Mechanics*, Vol. 897, 2020, p. A15. https://doi.org/10.1017/jfm.2020.367.

[15] Barth, H., Hein, S., and Rosemann, H., "Redesigned Swept Flat-Plate Experiment for Crossflow-Induced Transition Studies," *New Results in Numerical and Experimental Fluid Mechanics XI*, edited by A. Dillmann, G. Heller, E. Krämer, C. Wagner, S. Bansmer, R. Radespiel, and R. Semaan, Springer International Publishing, 2018, pp. 155–165.

[16] Lemarechal, J., Dimond, B. D., Barth, H. P., Hilfer, M., and Klein, C., "Miniaturization and Model-Integration of the Optical Measurement System for Temperature-Sensitive Paint Investigations," *Sensors*, Vol. 23, No. 16, 2023, p. 7075. https://doi.org/10.3390/s23167075.

[17] Kawakami, M., Kohama, Y., and Okutsu, M., "Stability characteristics of stationary crossflow vortices in three-dimensional boundary layer," *37th AIAA Aerospace Sciences Meeting and Exhibit*, 1999, pp. AIAA Paper A99–16660. https://doi.org/10.2514/6.1999-811.

[18] Gaponenko, V. R., Ivanov, A. V., Kachanov, Y. S., and Crouch, J. D., "Swept-wing boundary-layer receptivity to surface non-uniformities," *Journal of Fluid Mechanics*, Vol. 461, 2002, pp. 93–126. https://doi.org/10.1017/s0022112002008297.

[19] Yadala, S., Hehner, M. T., Serpieri, J., Benard, N., Dörr, P. C., Kloker, M. J., and Kotsonis, M., "Experimental control of swept-wing transition through base-flow modification by plasma actuators," *Journal of Fluid Mechanics*, Vol. 844, 2018. https://doi.org/10.1017/jfm.2018.268.

[20] Rius-Vidales, A. F., and Kotsonis, M., "Impact of a forward-facing step on the development of crossflow instability," *Journal of Fluid Mechanics*, Vol. 924, 2021, p. A34. https://doi.org/10.1017/jfm.2021.497.

[21] Zoppini, G., Westerbeek, S., Ragni, D., and Kotsonis, M., "Receptivity of crossflow instability to discrete roughness amplitude and location," *Journal of Fluid Mechanics*, Vol. 939, 2022, p. A33. https://doi.org/10.1017/jfm.2022.220.

[22] Merino-Martinez, R., Carpio, A. R., Pereira, L. T. L., Herk, S. v., Avallone, F., Ragni, D., and Kotsonis, M., "Aeroacoustic design and characterization of the 3D-printed, open-jet, anechoic wind tunnel of Delft University of Technology," *Applied Acoustics*, Vol. 170, 2020, p. 107504. https://doi.org/10.1016/j.apacoust.2020.107504.

[23] Schrader, L.-U., Brandt, L., Mavriplis, C., and Henningson, D. S., "Receptivity to free-stream vorticity of flow past a flat plate with elliptic leading edge," *Journal of Fluid Mechanics*, Vol. 653, 2010, pp. 245–271. https://doi.org/10.1017/s0022112010000376.

[24] Arnal, D., and Casalis, G., "Laminar-turbulent transition prediction in three-dimensional flows," *Progress in Aerospace Sciences*, Vol. 36, No. 2, 2000, pp. 173 – 191. https://doi.org/10.1016/S0376-0421(00)00002-6.

[25] Reed, H. L., Saric, W. S., and Arnal, D., "Linear Stability Theory Applied to Boundary Layers," *Annual Review of Fluid Mechanics*, Vol. 28, No. 1, 1996, pp. 389–428. https://doi.org/10.1146/annurev.fl.28.010196.002133.

[26] Mack, L., "Boundary layer linear stability theory," *Special Course on Stability and Transition of Laminar Flows*, 1984, pp. AGARD–R–709.

[27] Groot, K., "BiGlobal Stability of Shear Flows: Spanwise & Streamwise Analyses," Ph.D. thesis, Delft University of Technology, 12 2018. https://doi.org/10.4233/uuid:60ef07b2-00db-418b-9495-5a9baf6105df.

[28] Weideman, J. A., and Reddy, S. C., "A MATLAB differentiation matrix suite," *ACM Transactions on Mathematical Software (TOMS)*, Vol. 26, No. 4, 2000, pp. 465–519. https://doi.org/10.1145/365723.365727.

[29] Westerbeek, S., "Development of a nonlinear parabolized stability equation (NPSE) analysis tool for spanwise invariant boundary layers." , 2020.

[30] Haynes, T. S., and Reed, H. L., "Simulation of swept-wing vortices using nonlinear parabolized stability equations," *Journal of Fluid Mechanics*, Vol. 405, 2000, pp. 325 – 349. https://doi.org/10.1017/S0022112099007260.

[31] Hultmark, M., and Smits, A., "Temperature corrections for constant temperature and constant current hot-wire anemometers," *Measurement Science and Technology*, Vol. 21, No. 10, 2010, p. 105404. https://doi.org/10.1088/0957-0233/21/10/105404.

[32] Rius-Vidales, A. F., and Kotsonis, M., "Unsteady interaction of crossflow instability with a forward-facing step," *Journal of Fluid Mechanics*, Vol. 939, 2022, p. A19. https://doi.org/10.1017/jfm.2022.151.

[33] Downs, R. S., and White, E. B., "Free-stream turbulence and the development of cross-flow disturbances," *Journal of Fluid Mechanics*, Vol. 735, 2013, pp. 347–380. https://doi.org/10.1017/jfm.2013.484.

[34] Zoppini, G., Ragni, D., and Kotsonis, M., "Experimental Investigation on Receptivity of Crossflow Instability to Discrete Roughness Amplitude and Location," *AIAA Scitech 2021 Forum*, 2021, pp. AIAA Paper 2021–052. https://doi.org/10.2514/6.2021-0152.

[35] Malik, M. R., Li, F., and Chang, C., "Nonlinear crossflow disturbances and secondary instabilities in swept-wing boundary layers," *IUTAM Symposium on Nonlinear Instability and Transition in Three-Dimensional Boundary Layers (ed. P. W. Duck & P. Hall)*, 1996, pp. 257–266. https://doi.org/10.1007/978-94-009-1700-2_25.

[36] Wassermann, P., and Kloker, M., "Mechanisms and passive control of crossflow-vortex-induced transition in a three-dimensional boundary layer," *Journal of Fluid Mechanics*, Vol. 456, 2002, pp. 49 – 84. https://doi.org/https://doi.org/10.1017/S0022112001007418.

[37] Wassermann, P., and Kloker, M., "Transition mechanisms induced by travelling crossflow vortices in a three-dimensional boundary layer," *Journal of Fluid Mechanics*, Vol. 483, 2003, pp. 67–89. https://doi.org/10.1017/S0022112003003884.

[38] Welch, P., "The use of fast Fourier transform for the estimation of power spectra: a method based on time averaging over short, modified periodograms," *IEEE Transactions on audio and electroacoustics*, Vol. 15, No. 2, 1967, pp. 70–73.

[39] Deyhle, H., and Bippes, H., "Disturbance growth in an unstable three-dimensional boundary layer and its dependence on environmental conditions," *Journal of Fluid Mechanics*, Vol. 316, 1996, pp. 73–113. https://doi.org/10.1017/S0022112096000456.

[40] Serpieri, J., and Kotsonis, M., "Conditioning of unsteady cross-flow instability modes using dielectric barrier discharge plasma actuators," *Experimental Thermal and Fluid Science*, Vol. 93, 2018, pp. 305 – 318. https://doi.org/10.1016/j.expthermflusci.2018.01.007.

[41] Groot, K. J., Serpieri, J., Pinna, F., and Kotsonis, M., "Secondary crossflow instability through global analysis of measured base flows," *Journal of Fluid Mechanics*, Vol. 846, 2018, pp. 605–653. https://doi.org/10.1017/jfm.2018.253.